High Infrared Photoconductivity in Films of Arsenic-Sulfide-Encapsulated Lead-Sulfide Nanocrystals

Sergii Yakunin,[†,‡,§] Dmitry N. Dirin,[‡,§] Loredana Protesescu,[‡,§] Mykhailo Sytnyk,[†] Sajjad Tollabimazraehno,[⊥] Markus Humer,[†] Florian Hackl,[†] Thomas Fromherz,[†] Maryna I. Bodnarchuk,[‡,§] Maksym V. Kovalenko,[‡,§] and Wolfgang Heiss*[,†,∥,#]

[†]Institute of Semiconductor and Solid State Physics, Johannes Kepler University Linz, Altenbergerstraße 69, Linz 4040, Austria, [‡]Department of Chemistry and Applied Biosciences, ETH Zürich, Vladimir-Prelog-Weg 1, Zurich CH-8093, Switzerland, [§]Empa-Swiss Federal Laboratories for Materials Science and Technology, Uberlandstraße 129, Dübendorf CH-8600, Switzerland, [⊥]Zentrum für Oberflächen- und Nanoanalytik, University Linz, Altenbergerstraße 69, Linz 4040, Austria, [∥]Materials for Electronics and Energy Technology (i-MEET), Friedrich-Alexander-Universität Erlangen-Nürnberg, Martensstraße 7, 91058 Erlangen, Germany, and [#]Energie Campus Nürnberg (EnCN), Fürther Straße 250, 90429 Nürnberg, Germany

ABSTRACT Highly photoconductive thin films of inorganic-capped PbS nanocrystal quantum dots (QDs) are reported. Stable colloidal dispersions of $(NH_4)_3AsS_3$-capped PbS QDs were processed by a conventional dip-coating technique into a thin homogeneous film of electronically coupled PbS QDs. Upon drying at 130 °C, $(NH_4)_3AsS_3$ capping ligands were converted into a thin layer of As_2S_3, acting as an infrared-transparent semiconducting glue. Photodetectors obtained by depositing such films onto glass substrates with interdigitate electrode structures feature extremely high light responsivity and detectivity with values of more than 200 A/W and 1.2×10^{13} Jones, respectively, at infrared wavelengths up to 1400 nm. Importantly, these devices were fabricated and tested under ambient atmosphere. Using a set of time-resolved optoelectronic experiments, the important role played by the carrier trap states, presumably localized on the arsenic-sulfide surface coating, has been elucidated. Foremost, these traps enable a very high photoconductive gain of at least 200. The trap state density as a function of energy has been plotted from the frequency dependence of the photoinduced absorption (PIA), whereas the distribution of lifetimes of these traps was recovered from PIA and photoconductivity (PC) phase spectra. These trap states also have an important impact on carrier dynamics, which led us to propose a kinetic model for trap state filling that consistently describes the experimental photoconductivity transients at various intensities of excitation light. This model also provides realistic values for the photoconductive gain and thus may serve as a useful tool to describe photoconductivity in nanocrystal-based solids.

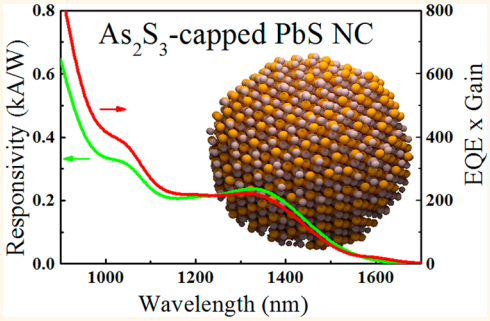

KEYWORDS: lead sulfide · nanocrystals · inorganic ligands · photodetectors · trap states

Colloidal semiconductor nanocrystals (NCs), also known as colloidal quantum dots (QDs) due to their size-tunable optical and electronic properties, are highly appealing for applications in light-sensing devices operating in the visible,[1−4] as well as in the near- and mid-infrared (IR),[5−16] spectral regions. In particular, QD-based photodetectors that operate in the IR region beyond wavelengths of 1000 nm have no equivalent Si-based counterparts. This has stimulated an immense interest in the development of IR-active NCs, including in their synthesis, surface functionalization, as well as their optical and electronic properties in colloidal solutions and in thin films.[17−20] Despite the general notion that colloidal NCs are easy to process into devices by solution-based techniques (including spray-, spin-, dip- or drop-casting), a common obstacle of this approach is the presence of bulky organic capping ligands on the NC surface after synthesis, which block the interparticle transport rendering all NC solids highly insulating. Thus, an additional step of ligand-exchange is required in order to improve charge transport, which can be carried out either after the film deposition by a so-called solid-state ligand exchange with small organic molecules,[15,21−31] or in solution-phase before the deposition of the NCs.[8,32] Solution-phase ligand-exchange

* Address correspondence to wolfgang.heiss@fau.de.

Received for review November 26, 2014 and accepted December 3, 2014.

Published online December 03, 2014
10.1021/nn5067478

with butylamine has led to the first observations of very high responsivities of up to 10^3 A/W and a detectivity of 1.8×10^{13} Jones in PbS NC solids.[8] Solid-state ligand-exchange strategies have received the greatest attention over the past decade and led, for instance, to the first examples of NC solids with electron mobilities reaching 1 $cm^2/(V\ s)$ and above,[25,28,30,33] efficient IR photodetectivities (PbS and HgTe NCs),[10,32] and, very recently, record-high power conversion efficiencies of 8% in QD photovoltaics.[34,35] In the last several years, a clear trend toward the use of small *inorganic* capping ligands has been observed, in both solid-state and solution-phase adaptations of ligand-exchange reactions.[36−50] Inorganic ligands are generally nonvolatile and are expected to yield stable, electronically pure NC solids with efficient and tunable electronic connectivity between NCs. Various atomic and complex anionic species can serve as inorganic capping ligands: halides (I^-, Br^-, Cl^-)[40−42] and pseudohalides (N_3^-, OCN^-, SCN^-),[47,49−51] metal-free chalcogenido, oxo- and amido species (S^{2-}, HS^-, Se^{2-}, HSe^-, Te^{2-}, HTe^-, TeS_3^{2-}, OH^-, NH_2^-),[39,44,52−56] oxo- and polyoxometallates,[57,58] halometallates (such as $CH_3NH_3PbI_3$),[36] and chalcogenidometallates ($Sn_2S_6^{4-}$, $In_2Se_4^{2-}$, or $Cu_7S_4^-$, AsS_3^{3-}, *etc.*).[37,38,43−46,55,59−61] Solution-phase or solid-state treatments of NCs with halide ions, providing partial surface coverage, have been reported by several groups,[40] leading to improved electronic passivation of semiconductor NCs, higher oxidative stability and high power conversion efficiencies in PbS NC-based photovoltaics of 6−7%.[62,63]

Of all aforementioned inorganic ligands, chalcogenidometalates have received the greatest attention due to their (for most cases) stronger binding affinity to NC surfaces, including metals (Au, Pd) and semiconductors (CdSe, PbS, InAs, InP, *etc.*), leading to fast and complete exchange of the native organic capping molecules. In highly polar solvents such as water or formamide (FA), these colloids are electrostatically stabilized due to the adsorption of anionic ligands onto the NC surface and electrostatic dissociation of counterions. With the integrity and size-tunable optical properties of NCs fully preserved, these colloids serve as highly pure (oxygen- and carbon-free) all-inorganic inks for depositing useful solid-state materials. Charge transport in solids comprising such all-inorganic NCs is greatly improved and high (for NC solids) electronic mobilities of 5−35 $cm^2\ V^{-1}\ s^{-1}$ are now routinely obtained.[1,44,50,52,61,64−66] These colloids have served as fully inorganic inks for solution-deposited $CuInS_2$, $Cu(In_{1-x}Ga_x)Se_2$ and $Cu_2ZnSn(S,Se)_4$ (CZTS) phases in applications as thin-film absorbers for photovoltaics.[43,67] Similar chemistries have enabled the preparation of ionically conductive composites of Ag_2S NCs embedded into a GeS_2 matrix,[68] and Sb_2Te_3-based nanocomposites for thermoelectrics,[69,70] as well as the integration of highly luminescent PbS/CdS NCs into fully inorganic IR-transparent matrices.[45]

Surface chemistry has a profound effect on nearly all electronic and optical characteristics of colloidal NCs, including electronic coupling/charge transport, doping levels and charge carrier trap states, luminescence lifetimes, *etc.*[1,2,7,8,15,21,23−25,36,38−42,44−46,52−54,71−76] Therefore, it is not a surprise that essentially all aforementioned reports on photoconductivity in NC solids have illustrated an intimate relationship between the photoconductive properties (responsivity, detectivity, rate-capability, *etc.*) and the surface chemistry. So far, very little is known about the photoconductive properties of inorganic-capped NCs. High photoconductivity in the visible spectral region has been reported for In_2Se_3-capped CdSe/CdS colloidal NCs, with detectivities reaching 10^{13} Jones.[77] The only report dealing with IR photodetectors with fully inorganic NC surface design has concerned HgTe NC films treated with As_2S_3 solutions in propylamine.[7] These films were reported to provide only a moderate responsivity of 5 mA/W, but over a very long wavelength range of up to 3.8 μm.

In this study, we explore the potential of inorganic-ligand-capped semiconductor NCs for light detection in the IR spectral region. To achieve the broadest context within the existing work in this field, the "classic" IR QD material, PbS NCs, was employed, also to take advantage of its compelling properties such as precisely tunable bandgap energies in the near-IR spectral region and high oxidative stability. PbS NCs have been combined with $(NH_4)_3AsS_3$ (ammonium thioarsenite or ammonium sulfidoarsenite) as the inorganic capping ligand. Sulfido-arsenites have been previously identified as the chalcogenido-based ligand with the highest binding affinity to the PbS surface.[37] In comparison to Na^+ and K^+ sulfide-arsenite salts, the ammonium analogue, $(NH_4)_3AsS_3$, can serve as a thermally degradable ligand, yielding arsenic(III) sulfide (As_2S_3) upon heating to 100 °C and above.[45]

We report that thin films of As_2S_3-capped PbS NCs, obtained under ambient air conditions by dip-coating from $(NH_4)_3AsS_3$−PbS NC colloids, exhibit outstanding responsivity and detectivity of more than 200 A/W and 1.2×10^{13} Jones, respectively, at IR wavelengths of around 1300 nm. Through a specially designed set of time-resolved optoelectronic experiments, the important role played by the carrier trap states, presumably localized on the arsenic-sulfide surface coating, has been uncovered. We also propose a kinetic model for trap state filling that consistently describes the experimental photoconductivity transients at various intensities of the excitation light.

RESULTS AND DISCUSSION

Colloidal NCs of PbS capped with oleate ligands were synthesized using the well-known procedure of Hines *et al.*[78] $(NH_4)_3AsS_3$-capped NCs were produced *via* a solution-phase ligand-exchange reaction, as previously described[45] (see Methods section for details).

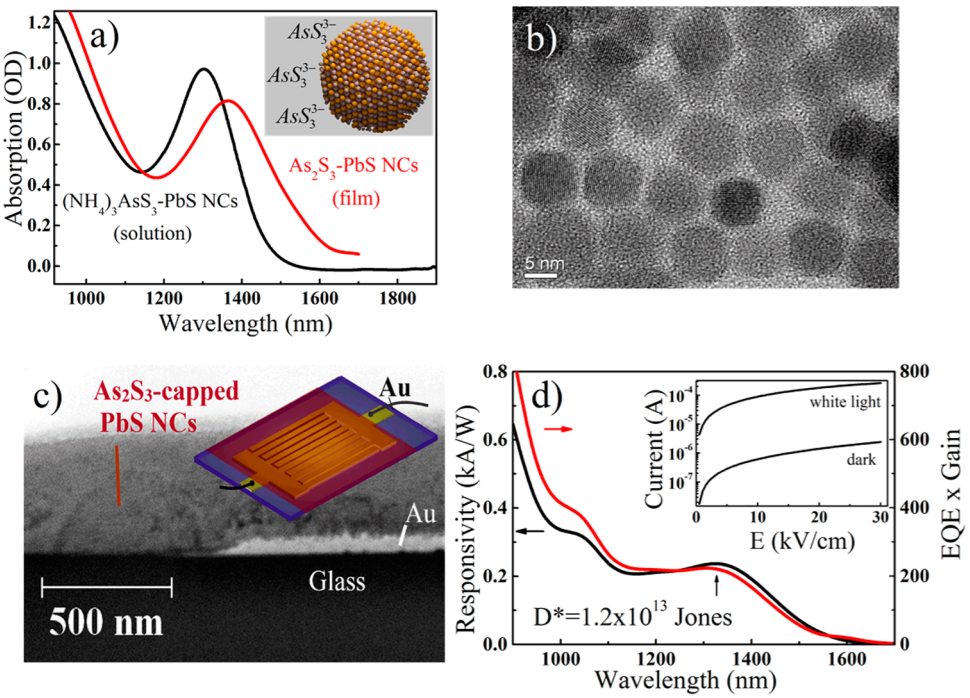

Figure 1. Photodetector preparation and characteristics. (a) Absorption spectra of a DMSO solution (black) and 20 layer thick film (red) of PbS NCs capped with AsS_3^{3-} ligands. The inset shows a model sketch of a PbS NC with attached AsS_3^{3-} ligand groups. (b) TEM image of a monolayer of PbS NCs capped with As_2S_3. (c) SEM cross-sectional image of a 20 layer PbS/As_2S_3 film, deposited on glass substrate for photoconductivity measurement. The inset shows a sketch of the substrate with an interdigitated gold electrode, covered by a PbS/As_2S_3film. (d) Responsivity (black) and product of EQE and gain (red) spectra for a 20 layer PbS/As_2S_3 film. The arrow indicates the excitonic peak for which the detectivity value is given. The inset shows the IV characteristics of the same sample.

An optical absorption spectrum of PbS NCs stabilized with $(NH_4)_3AsS_3$ and dispersed in dimethyl sulfoxide (DMSO) is presented in Figure 1a. The spectrum exhibits an excitonic peak at 1260 nm, characteristic of a mean particle size of 4.3−4.4 nm.[79] Thin films of PbS NCs were then obtained by dip-coating. A glass substrate was immersed into a DMSO solution of PbS NCs and pulled out with a speed of about 2 mm/s, followed by a drying step performed for 10 min at 130 °C, leading to the absorption of 2−3 monolayers of PbS NCs. This elevated temperature also induced the decomposition of the surface-bound $(NH_4)_3AsS_3$ into amorphous As_2S_3 (arsenic(III) sulfide).[45] For this reason, we refer to the thus-obtained thin film material as "As_2S_3-capped PbS NCs" or "PbS/As_2S_3" to highlight the differences between the thin surface films of As_2S_3 after dip-coating and the initial $(NH_4)_3AsS_3$ capping agent in solution. The procedure was repeated 20 times in order to obtain films with an optical density between 1 and 1.5 at the excitonic peak, which we found to be optimal for IR photoconductivity measurements. The absorption spectrum of a 20-layer thick film is presented in Figure 1a. The spectrum shows an excitonic peak at 1360 nm, considerably red-shifted and broadened in comparison to the excitonic absorbance measured in solution. Such behavior is commonly reported in films of PbS NCs with small-molecule ligands, and has been attributed either to an effective electronic coupling between NCs,[1,72] or to an increase of disorder combined with partial agglomeration in the film.[7] Very dense packing, with NC-NC spacings of less than 1 nm can be seen by transmission electron microscopy (TEM) in a single layer of PbS NCs with a size of 9 ± 1 nm, deposited onto a carbon-coated TEM grid (Figure 1b). This distance between NCs is notably shorter than the 2−2.5 nm spacing between NCs capped with long-chain oleate ligands. A detailed inspection of TEM images (Figures S1a−d, Supporting Information) also indicates larger interparticle gaps and voids, which are presumably filled by As_2S_3. Cross-section scanning electron microscopy (SEM) images (Figure 1c) of a 20-layer film indicate a uniform thickness of *ca.* 500 nm. For studying the photoconductive properties, identical films were deposited onto interdigitate electrodes deposited onto glass substrates (40 nm Au on 10 nm Ti, the total length of the electrodes is 8 mm, the gap between the electrodes was either 5 or 10 μm, Figure 1c). The photoconductivity and detectivity of the devices were measured as described in the Methods section. All experiments, from synthesis to device characterization, were conducted in air.

The inset of Figure 1d presents I−V dependencies in darkness and under illumination with white light. In darkness the conductivity of the sample is 2×10^{-6} S/cm, and it increases by 2 orders of magnitude under

illumination with an intensity of 20 mW/cm^2. With the measured carrier mobility (mobility measurements are described in detail below) these conductivity values correspond to hole concentrations of 8×10^{14} cm^{-3} in darkness and 4.5×10^{16} cm^{-3} under light. The spectral response curve (Figure 1d) was obtained with a bias of 60 kV cm^{-1} under illumination with monochromatic light with an intensity of about 15−30 μW/cm^2. The responsivity spectrum, measured at a modulation frequency of 1 Hz, closely reproduces the features of the absorption spectrum in that there is an excitonic peak at a wavelength of 1350 nm. In addition, there is a shoulder toward longer wavelengths in both absorbance and photoconductivity spectra. At the excitonic peak, the responsivity reaches 230 A/W for an illumination intensity of 30 μW/cm^2 and increases to *ca.* 450 A/W when the light intensity is reduced to below 1 μW/cm^2. The measured noise of the sample was 5 pA·(Hz)$^{1/2}$ with which a very high detectivity of 1.2×10^{13} Jones has been estimated. At low illumination intensities on the order of nW/cm^2, the responsivity reaches 10^3 A/W. These high photoresponse values point to a high product of external quantum efficiency (EQE) and photoconductive gain (G). Obviously, the EQE cannot exceed unity except in the case of multiexciton-generation contributing to photocurrent, which is efficient only when the ratio of photon-to-bandgap energies exceeds 2.5−2.7.[80] We therefore estimate that a high photoconductive gain of ~200 induces the high sensitivity of the detectors and is caused by the existence of only one type of mobile carriers (holes, as will be shown) and the trapping of the other type of carrier.

To investigate carrier trapping and carrier-escape-dynamics, we performed a wide range of frequency dependent and time-resolved experiments. With increasing modulation frequency, the photoconductivity, measured under monochromatic illumination (λ = 1440 nm) from an IR light-emitting diode (IR LED), monotonically decreases with increasing light modulation frequency (Figure 2a). The detectivity, in turn, shows a maximum between 200 and 300 Hz since the noise decreases with increasing frequency (Figure S2) faster than the photoresponse signal. Thus, the best signal-to-noise ratio of the PbS-As_2S_3 film is found in a frequency region which is useful for video imaging applications. By recording transient photocurrent traces excited by pulses of the IR LED of different durations, a rather unusual behavior is observed (Figure 2b). It can be seen that the decay time of the photocurrent transients strongly depends on the duration of the excitation pulses; the longer the excitation pulses are, the longer the relaxation time is. Interestingly, at higher illumination intensities the higher light fluency results in drastically different behaviors. Namely, for relatively short light pulses (t_{pulse} ~1 ms) the decay time is found to be almost independent of

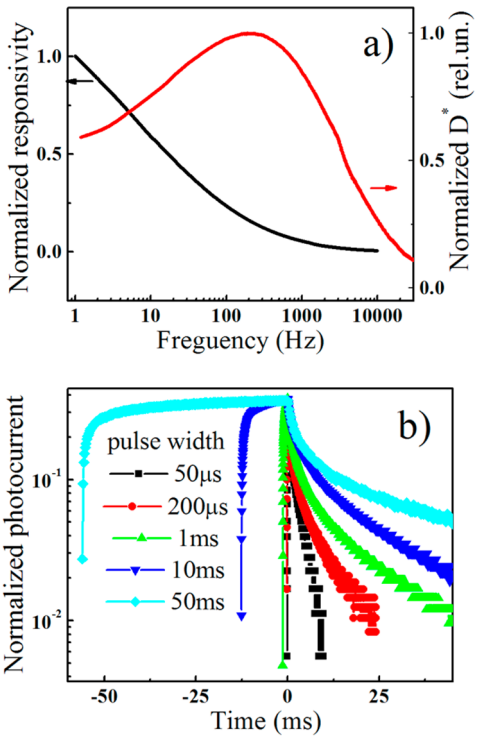

Figure 2. Modulated photoconductivity experiments. (a) Responsivity (black) and detectivity (red) measured at a wavelength of 1300 nm as a function of modulation frequency. (b) PC transients at a wavelength of 1300 nm, for light pulses durations in between 50 μs and 50 ms.

light intensity (see Figures S3 and S4). Further, for long pulses (t_{pulse} >100 ms) the decay time decreases with increasing light intensity. Thus, the observed decay time obviously depends on the fluency or the number of absorbed photons, rather than only on the light intensity.

To understand this behavior, we have performed further experiments to study the photoconductivity (PC) response of As_2S_3-capped PbS QDs after light absorption. We applied several time-resolved techniques, time-resolved photoluminescence, pump−probe (Figure S5) and photoinduced absorption (Figure S6), in order to reveal the nature of the nontrivial pulse-width dependence of the PC.

First it is noted that the photoluminescence (PL) intensity of the PbS NC films with As_2S_3 capping is strongly reduced compared to films with oleate capping. The PL spectrum shows a single excitonic peak and the PL cutoff on the long wavelength side of the spectrum is identical to that observed for films of oleate capped NCs (Figure S7). The shaded portion of the emission spectrum in the inset of Figure 3a was studied by transient PL spectroscopy. For the oleate-capped PbS NCs, a monoexponential decay is observed with a time constant of 60 ns, whereas with the inorganic ligands a substantially faster and biexponential decay occurs, described by two decay times of 500 ps and 2.5 ns. We ascribe this PL quenching to a

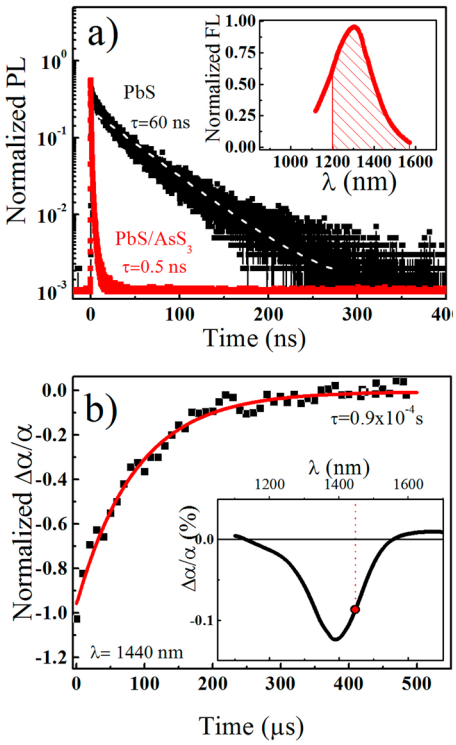

Figure 3. Carrier dynamics. (a) Time resolved fluorescence traces of oleate-capped PbS NCs (black) and As_2S_3-capped PbS NCs (red). The portion of the PL spectrum used for the time-resolved experiment is shaded in the PL spectrum, shown in the inset. Pump−probe trace for PbS/AsS_3^{3-} film recorded with a probe at 1440 nm. Black points, experiment data; red curve, exponential fit. Inset: PIA spectrum of a PbS/As_2S_3 film. The red point indicates the probe-wavelength from the transient experiment.

fast transfer of one of the photoexcited charge types from the PbS NCs to interfacial trap states. This charge trapping is apparently significantly faster than radiative recombination within the NCs. Since the field-effect transistor (FET) measurements discussed in further detail below provide p-type conductivity for both the intrinsic and light induced charge transport, which is presumably due to the known p-doping effect of atmospheric oxygen,[1,23,39,42,51] it can be deduced that electrons are the trapped type of carriers.

With transient photoinduced absorption (PIA), the opposite process was studied: namely, the escape of the electrons from the trap states. By steady state PIA of the As_2S_3-capped PbS QDs, a photoinduced bleach of the PbS excitonic transition is observed as a main feature (Figure 3b). The intensity of this bleaching is also related to the time the electrons reside at these states (referred to herein as the trap state escape time). We directly measured the escape time by a pump−probe experiment where the sample was pumped by 10 ps laser pulses at λ = 1064 nm and probed by electronically synchronized LED pulses at λ = 1440 nm (see the experimental setup in Figure S5). The probe pulse duration was 10 μs, and the delay time was varied between 0 and 500 μs. The pump−probe transient in Figure 3b shows the recovery of the photoinduced bleaching. It is fitted by an exponential function with a single rise time of τ = 90 μs. This value is on the same order of magnitude as the shortest values observed by the transient PC measurements shown in Figure 2b, indicating that the trap state escape time, measured here by pulsed pump−probe experiments, is a relevant parameter which determines the dynamics of the PC signals.

A high photoconductive gain was previously explained by surface trap states that appear on PbS due to partial oxidation.[76] Similar trap states also appear after ligand exchange with short organic,[73] or inorganic molecules,[40,46] when the PbS NCs lose their passivating oleate capping layer. The energy distributions of these trap states were investigated by the temperature dependences of PC transients,[74] and by mid-IR pump−probe experiments.[40] From pump−probe measurements the trap states were determined to be 0.1−0.3 eV below the PbS NCs conduction band, with a wide distribution over energy. Here the trap state distribution is investigated for the first time for inorganic chalcogenidometalate ligands. Photoinduced absorption spectroscopy was chosen as the experimental technique, where the optical density of the As_2S_3-capped PbS QD film was modulated by state filling effects, due to excitation by laser irradiation at a wavelength of λ = 532 nm, far above the band gap. In particular, we recorded the complex value of the modulated absorption response (Figure S6) including magnitude and phase information. We used different modulation frequencies (80 Hz and 20 kHz) to discriminate between fast responding QD-states and slower responding trap states. The fast component measured at 20 kHz exhibits a peak which is close to the excitonic absorbance maximum of the same film. The phase of the PIA response shows an almost rectangular shape, where the abrupt step between 180° and 0° indicates the transition between photoinduced bleaching and photoinduced absorbance. The abruptness of this transition, while all other regions are rather flat, indicates that the response of all involved transitions is faster than the time given by the modulation frequency (*i.e.*, 50 μs). The PIA spectrum measured at 80 Hz (shown in Figure 4a) is broader than the spectrum measured at 20 kHz and this broadening expands toward longer wavelengths. This is because the spectrum with 80 Hz modulation is more sensitive to slow responding states, whereas a modulation of 20 kHz acts like a high-pass filter. Thus, the response of the slow component can be extracted from the data by subtracting the 20 kHz data from the 80 Hz data, providing us the magnitude and phase of the slow components only (green line in Figure 4a,b). The magnitude of the slow component represents the density distribution of the trap states. While the large width of this trap state distribution function covering

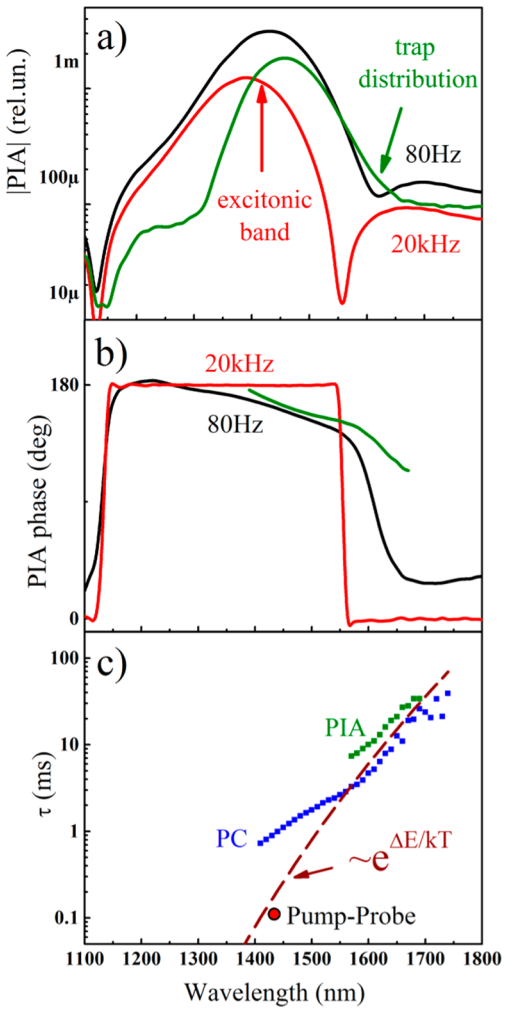

Figure 4. Trap states: distribution and lifetimes. (a,b) PIA amplitude and phase spectra, measured at two light modulation frequencies (80 Hz, black; 20 kHz, red). The difference between these spectra shown in green corresponds to the slow component of the PIA and represents the product of trap density distribution $N(\lambda)$ and light absorption cross-section $\sigma(\lambda)$. (c) From (b) and eq 1 the electron trap state escape time distribution is calculated (green). The same time evaluated from the PC response phase of Figure S9 is given in blue. The dashed line represents eq 2, and the same data are shown on Figure S10 on a Arrhenius plot. The lifetime deduced from the pump−probe experiment, red point, fits well to the prediction of eq 2.

wavelengths between 1350 and 1600 nm does not allow one to specify the exact nature of the trap states, we can rule out that they are generated solely by partial oxidation since oxidation results in substantially deeper trap states (see Figure S8). Remarkably, the sign of the slow component is always negative (the phase is higher than 90°) and thus the photoinduced bleaching is caused by the transient population of trap states by electrons. The absorbance modulation due to laser excitation induced trap state filling amounts to approximately 1% of the linear absorbance measured at these wavelengths. The phase signal of the trap state photoinduced absorbance exhibits a clear trend: with increasing wavelength, the corresponding phase is increasingly delayed behind the excitation pulse. This phase delay can be directly recalculated as a time which can be interpreted as the lifetime of the electrons in the trap states, or, in other words, as their escape time:

$$\tau(\lambda) = \frac{-\tan(\mathrm{Arg}(\mathrm{PIA}(\lambda)))}{f\ [\mathrm{Hz}]} \quad (1)$$

This is shown as green points in Figure 4c. Similar phase delays were also observed in the photoconductivity experiments (Figure S9). From the latter experiments, the escape times calculated by eq 1 correspond to the photoconductive states, presented as blue points on Figure 4c. We must note that the modulation method allows the extraction of characteristic times, which are grouped by 1 order of magnitude around the modulation period. For the frequencies used (~100 Hz), characteristic times between 1 and 100 ms are deduced. This is the reason why the escape times deduced from the photoconductivity spectrum (120 Hz modulation frequency) show two different dependencies. Between wavelengths of 1550 and 1750 nm, a continuous increase of escape time with wavelength is observed on logarithmic scale. Toward shorter wavelengths, however, this dependence diverges since the experimental data reach the lower limit of the time window provided by the 120 Hz modulation technique. The data for the escape times deduced from the slow components of the PIA experiments level off at an even higher value since all of the fast components were removed by the subtraction used to generate these data. For escape times longer than 10 ms, however, a good agreement between escape times from PC and PIA experiments is found. Within this time range, the deduced electron lifetimes in the trap states can be compared to the theoretically predicted dependence of trap lifetimes as a function of trap energy:[81]

$$\tau(\Delta E) \approx e^{\Delta E/kT} \quad (2)$$

This comparison is shown by the dashed line in Figure 4c and in Arrhenius form with the trap state binding energy on the *x*-axis in Figure S10. As shown, eq 2 fits well to the escape times deduced from photoinduced absorption and transient photoconductivity between 10 and 100 ms. The trap state binding energy, ΔE, is measured here with respect to the exciton-energy, or in other words, to the peak of the fluorescence. For traps with binding energies below 100 meV (wavelengths below 1550 nm) the electron escape time is below the resolution of the PIA and transient PC setup. Therefore, for the estimation of the electron lifetime in shallow traps, we applied the pump−probe method described above and detailed in the Methods section. The photoinduced absorption transient measured at a wavelength of 1440 nm, corresponding to a trap binding energy of 40 meV, provides a trap state escape time of about 90 μs. Again, this fits very well to the thermal relationship between electron escape time and trap

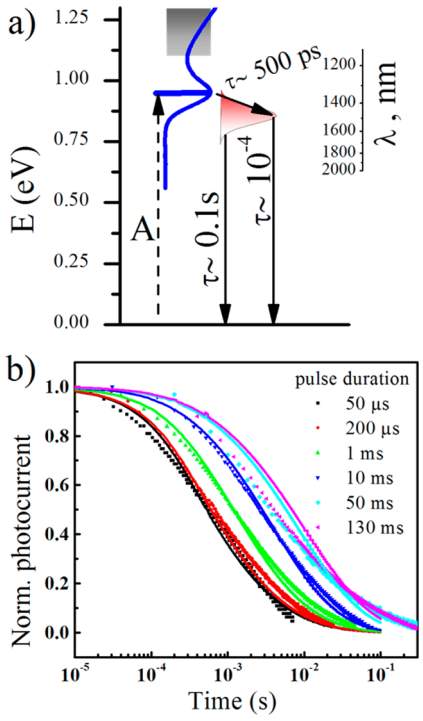

Figure 5. Carrier dynamics model and fit to experiment. (a) Sketch of energy diagram where the arrows describe light absorption A, electron trapping (time constant $\tau \sim$ 500 ps) and escape (arrows with time constant τ 0.1 ms to 0.5 s) from trap states with different binding energies. (b) Photoconductivity decay transients after light pulses with various durations. The symbols are the experimental data from Figure 2b, whereas the lines are fits obtained with eq 6.

state binding energy described by eq 2 (see Figure 4c and S10).

The set of experimental data described above gives clear evidence as to the origin of the high photoconductive gain observed in the As_2S_3-capped PbS NCs films. Upon photoexcitation of an electron−hole pair, the electron quickly becomes trapped (Figure 5a), giving the hole the possibility to contribute to the photocurrent until the electron escapes from the trap state and recombines with the hole. Thus, the photoconductivity is proportional to the number of trapped electrons; however, each trapped electron contributes to the photoconductivity differently, according to its escape time. This dependence has to be considered to account for the intensity dependence of the photoconductivity transients, which is observed in the response to light pulses $I(t)$ ($I(t) = I_0$ for a time interval between $-t_p$ and 0, and $I(t) = 0$ otherwise).

To calculate the photoconductivity transients, the number of trapped electrons has to be evaluated. This is performed here by an expanded two level rate equation model with a common ground state and a set of independent excited states. The excited states are grouped into subsets of states providing the same electron escape time, τ. The total number of electrons in the excited states per time interval dt, d$n_{excited}$, is provided by photon absorption, and is thus described by the absorption cross section, σ by the light intensity, $I(t)$, and the number of electrons in the ground state, n_{ground}. (d$n_{excited}$ = $I(t)\sigma n_{ground}$ dt). These electrons are distributed among the subsets of electronic states according to the trap state density distribution function, $N(\tau)$, *via* the approximate relationship: d$n_{trapped}(\tau) \approx$ d$n_{excited}N(\tau)$. Assuming that the excited states are noninteracting, the carrier escape from each subset of trap states follows: $-$d$n_{trapped}$ = $(1/\tau)n_{trapped}$ dt. This provides a linear differential equation for $n_{trapped}(t)$ and the approximate analytical solution is given in Supporting Information (eqs S1−S7) for a given value of τ. The photoconductivity signal is then obtained by integrating over the number of electrons in all excited states, *i.e.*, over all subsets with different trap state escape times. Within the time interval of the light pulse, this integral is given by

$$\mathrm{PC}(t) \approx n_{trapped}(t) = \int_{\tau 1}^{\tau 2} \tau I \sigma N(\tau) \left[1 - \exp\left(\frac{-(t - t_p)}{\tau}\right)\right] \mathrm{d}\tau \quad (3)$$

where τ_1 and τ_2 are the extremes of the experimentally measured electron escape times from the trap states (100 μs and 0.5 s). The trap state distribution function $N(E)$ was experimentally determined from the frequency dependent PIA experiments as a function of the trap state binding energy (Figure 4a), which can be easily rewritten into a trap state escape time dependence $N(\tau)$ (Figure S11) by making use of their relation to each other, provided by eq 2. Inserting this result into eq 3 describes the measured data well at low light intensities. However, under intense illumination, the fact that the total number of trap states is finite becomes important since it results in saturation effects. The photoinduced bleaching measured by PIA experiments is caused by saturation and we include it in the mathematical description by a phenomenological term,[82] which in this case depends on two parameters: the saturation intensity, I_{sat}, and a saturation relaxation time, τ_{sat}. Thus, eq 3 is modified to

$$\mathrm{PC}(t) \approx n_{trapped} = \int_{\tau 1}^{\tau 2} \tau I \sigma N(\tau) \frac{1 - \exp(-(t - t_p)/\tau)}{(1 + \tau I \sigma N(\tau)/(I_{sat}\exp(-\sqrt{\tau/\tau_{sat}}))} \mathrm{d}\tau \quad (4)$$

This is an appropriate expression to fit the experimental photoconductivity transients for various intensities. Here, it is taken that each subset of excited states provides different saturation intensities. This dependence of the saturation energy is described by the saturation term: $\exp(-(\tau/\tau_{sat})^{1/2})$. This reveals that the longer the electron escape time is, the more easily the corresponding optical transition can be bleached. The particular shape of this function was obtained from a fit of the long-living tail of the trap state distribution *vs*

lifetime, presented in Figure S11. Since the saturation term affects predominantly long-living traps, only under excitation with long pulses were saturation effects observed, whereas for short pulses they were completely absent. In Figure S12 it is seen that eq 4 provides a reasonably good fit of the rising part of the photoconductivity transients measured with either 1 or 100 ms long light pulses and an intensity of 40 mW/cm^2 and 0.4 W/cm^2, respectively. These fits also provide the two fit parameters: the saturation intensity, I_{sat} = 70 W/cm^2, and the saturation lifetime, τ_{sat} = 0.5 ms.

For the decay part of the photoconductivity transients ($t > 0$), we used the same set of equations describing the expanded two level system. However, in this case, as a starting point of the decay curve, the number of occupied trap states at the time of the pulse end ($t = 0$) must first be evaluated for each electron escape time τ, which can obtained by using eq S7:

$$n_{trapped}(t = 0) = \tau I \sigma n_{ground} N(\tau) \left[1 - \exp\left(\frac{t_p}{\tau}\right)\right] \quad (5)$$

After the light pulse is over, the number of trapped electrons exponentially decays from each subset of trap states according to its escape time, τ. Again, the photoconductivity is obtained by integrating the electron densities over all subsets dτ:

$$PC(t) \approx n_{trapped}(t) = \int_{\tau 1}^{\tau 2} \tau I \sigma N(\tau) \left[1 - \exp\left(\frac{-t_p}{\tau}\right)\right] \exp\left(\frac{-t}{\tau}\right) d\tau \quad (6)$$

This expression provides consistent fits for all decay parts of the photoconductivity transients shown in Figure 2b, measured for light pulse durations between 50 μs and 100 ms (shown in Figure 5b on a logarithmic scale). Qualitatively, it reproduces the experimentally observed increase of the photoconductivity decay time with increasing light pulse duration. Quantitatively, the fits are better for short light pulses whereas the errors increase slightly with increasing light pulse duration. In this respect, some refinements of the simple model applied here might be possible.

While the *photoconductivity provides the product of quantum efficiency and photoconductive gain*, the value of the latter is rarely directly determined. The photoconductive gain is known to be the ratio between the escape time of the trapped carriers and the transit time of the mobile carrier type: $G = \tau/t_{tr}$. While the escape time was determined above by several methods and was shown to depend on the binding energy of the trap states, the transit time has to be determined independently from mobility experiments, *via* $t_{tr} = L^2/(\mu V)$. Here, L is the sample length and V is the applied voltage. The mobility was determined from field-effect transistor measurements, performed directly on the photodetector samples. For that purpose, a top-gate was fabricated on the 500 nm thick As_2S_3-capped PbS NC film, consisting of a 20 nm dielectric layer of Al_2O_3 (deposited by atomic layer deposition) and a 50 nm thick Au electrode. The transistor characteristics in darkness and under white light illumination is presented in Figure S13a,b, respectively. p-type conductivity is shown in both darkness and under illumination (20 mW/cm^2). The mobility values were determined from the linear part of the transfer characteristics, following the method described elsewhere.[83] The obtained hole mobilities of 0.016 (in darkness) and 0.034 cm^2/(V s) (under illumination) correspond to transit times in the range of 3−6 μs.

To evaluate the gain value, where the trap escape times from the PIA experiments are used as the carrier lifetime, the trap escape time is averaged over the trap state distribution density ($\langle\tau\rangle = \int N(\tau)\tau\, d\tau / \int N(\tau)\, d\tau$). A value of τ = 1.8 ms is obtained as a weighted average, which, together with the transit time from the FET measurements, provides a photoconductive gain value between 150 and 300. This value fits very well to the product of the optical gain and EQE (200), deduced from the responsivity spectrum in (Figure 1d) at a wavelength of 1440 nm, which was applied in the investigation of the transient photoconductivity. While these values are relevant for low excitation intensities, with increasing intensity the averaged trap state escape time is decreased by saturation effects. This decrease is consistent with the deduced specific relaxation time parameter τ_{sat} from the transient photoconductivity experiments, which is considerably shorter than the averaged trap state escape time $\langle\tau\rangle$ deduced at low intensities. Thus, with increasing light intensity, the gain decreases similarly as was reported in other NC photodetectors.[74] In addition, the strong increase of the responsivity with decreasing modulation frequency is consistently explained by the dependence of the photoconductive gain from the trap state lifetimes. As shown above, the longer the light pulses are, the longer the trap-state escape times can be. These long trap state escape times result in the extremely high photoresponsivity observed here at low modulation frequencies.

CONCLUSIONS

Finding an appropriate ligand is of utmost importance for the optimization of NC films for light harvesting devices and photodetectors. Here, photoconductors made of PbS NCs capped with As_2S_3 thin layers *via* thermal decomposition of $(NH_4)_3AsS_3$ were presented, exhibiting extremely high light responsivity and detectivity values of more than 200 A/W and 1.2 × 10^{13} Jones, respectively, in the IR spectral region (λ = 1300 nm). This high performance is enabled by a combination of high photosensitivity of the PbS QDs and effective charge transport. While the former is related to carrier trapping, which also causes the high

response to be observed at low frequencies only, the latter is due to the inorganic capping that reduces the distances between NCs, and acts as an IR-transparent semiconducting matrix. Unlike the highly sensitive PbS NC based photoconductors prepared with short organic ligands[8], the photodetectors presented in this work were prepared, stored and measured in ambient air, where they showed stable operation over several months. On the basis of results from transient fluorescence, photoinduced absorbance, and photoconductiviy experiments, as well as complementary frequency dependent studies, a simple rate equation model was developed and was shown to be consistent with experiments. In addition, the trap state distribution function was deduced, which is not only an important part of the rate equation model, but is also required, for instance, to properly evaluate weighted average values of the electron trap state escape time. With this, and the carrier transit times deduced from field-effect transistor experiments, a realistic value of **200** for the photoconductive gain was deduced. Thus, the applied model is a powerful tool for describing photoconduction in NC devices, which are often governed by carrier trapping into states with a wide range of binding energies.

METHODS

Preparation of $(NH_4)_3AsS_3$-Capped PbS NCs. Colloidal oleate-capped PbS NCs were synthesized as described by Hines at al.[78] In a three-neck reaction flask, $PbAc_2 \times 3H_2O$ (2 mmol, 0.758 g, 99,99%, Sigma-Aldrich), octadecene (ODE,10 mL, techn. grade, Sigma-Aldrich) and oleic acid (10 mL, 90% Sigma-Aldrich) were dried at 120 °C under a vacuum for 1 h to dissolve lead salt and to dry the solution. The temperature was then raised to 145 °C. In a glovebox, a sulfur precursor solution was prepared by mixing bis(trimethylsilyl)sulfide (TMS_2S, 0.21 mL, 1 mmol, Aldrich, synthesis grade) with dried ODE (10 mL). The sulfur solution was quickly injected into the reaction flask, which is kept at 145 °C. Three minutes later, the heating mantle was removed from the reaction flask and an ice−water bath was used to cool its content down to room temperature. The isolation and purification procedure was carried out in air. Hexane (20 mL) and ethanol (20 mL) were added to the crude solution, followed by centrifugation to separate the NCs. The PbS NCs were redispersed in hexane (20 mL), and precipitated again with ethanol (20 mL). This procedure was repeated 3 times and the PbS NCs were finally redispersed in toluene.

$(NH_4)_3AsS_3$[45,84] was prepared by dissolving As_2S_3 (0.492 g, 99,999%, Alfa-Aesar) in a solution containing $(NH_4)_2S$ (0.86 mL, 40−48% in water, Sigma-Aldrich) and 10 mL of H_2O at room temperature, forming a colorless solution. Solid $(NH_4)_3AsS_3$ was precipitated by adding acetone, isolated by centrifugation and rinsed with acetone. We note that $(NH_4)_3AsS_3$ slowly decomposes to As_2S_3 at room temperature in the course of several days and therefore has to be freshly prepared before the use for surface functionalization of PbS NCs.

$(NH_4)_3AsS_3$-capped PbS NCs were prepared as described in ref 45: The formamide (FA) solution of $(NH_4)_3AsS_3$ (10 mL, 5.5 mg/mL) and the toluene solution of oleate-capped PbS NCs (10 mL, 3 mg/mL) were combined and stirred in the same vial at room-temperature until the ligand exchange was complete (NCs are fully transferred in the FA solution and the toluene solution is clear after phase separation), which usually took 60 min. The FA phase was rinsed 3 times with hexane and then the particles were flocculated by adding acetonitrile (10 mL). $(NH_4)_3AsS_3$-capped PbS NCs were redispersed in FA (2 mL), precipitated one more time, and redispersed in FA or DMSO (1 mL).

Deposition of the Films of As_2S_3-Capped PbS NCs for Photoconductivity Measurements. Substrates with interdigitated electrodes were prepared on glass substrates by optical lithography, thermal evaporation, followed by a lift-off process. The electrodes are films of Au/Ti with 40/10 nm thicknesses. The size of the gap between electrodes was varied between 5 and 20 μm and its total length was 8 mm. Shortly before depositing PbS NCs, the substrates were cleaned by sonication in acetone followed, by a treatment with an oxygen plasma. Solid films of As_2S_3-encapsulated PbS NCs were deposited by dip-casting. For that purpose DMSO solutions were used, in which the substrates were immersed and pulled out with a controlled speed of 2 mm/s. After each deposition step the substrates were dried for 10 min at 130 °C under ambient air. This procedure was repeated 20 times in order to deposit films of reasonable optical absorbance in the infrared region of the exciton transition. All reference samples were prepared in the same way.

Characterization Methods. *Electron Microscopy.* Transmission electron microscopy (TEM) images were recorded using a Tecnai F30 microscope operated at 300 kV. Carbon-coated copper TEM grids (type-B, Ted Pella) were used as substrates. For cross-sectional investigations of the NCs films the film was cut with focused ion beam (FIB) using Ga ions from a ZEISS 1540XB Crossbeam microscope. The cross section was polished by using subsequently decreasing beam currents down to 50pA (at 30 kV acceleration voltage).

Photoconductivity. measurements were performed by illumination with a tungsten lamp, monochromatized by an Acton SP2150 (Princeton Instruments) spectrograph/monochromator. The light was modulated by a mechanical chopper within a frequency range from 2 to 120 Hz. Bias was applied by a Keithley 236 SMU with 10−20 V, chosen according to the stability of the dark current. The signal, amplitude and phase, was recorded by a Stanford Research lock-in amplifier. The setup was controlled by a home-written software in LabView. IV characteristics were measured by the Keithley 236 SMU with and without illumination of a tungsten lamp. Frequency dependencies (recorded on lock-in) and PC transients (recorded on a digital storage Tektronix TBS1102 oscilloscope) were obtained with a load resistance of 50 Ohm and pulsed focused illumination from a LED1300E (Thorlabs) with a center wavelength of 1300 nm. Noise measurements were performed by a lock-in amplifier according to the procedure described in ref 8. In this case the sample was mounted in a metallic shielding box, and the bias was applied from a battery.

Field Effect Transistors. For field-effect transistor (FET) experiments the photoconductivity sample with a 500 nm thick NC film was covered by a 20 nm top dielectric layer of Al_2O_3 and a 50 nm thick Au film as gate electrode. Transistor characteristics were recorded with grounded source: 2 Keithley 236 SMUs were used to control and measure current/voltages *via* gate and drain. Transistor characteristics were recorded in dark and under white light illumination with 20 mW/cm^2.

Absorption Spectra. of NC solutions were recorded with a Jasco V670 spectrophotometer, and from NC films with an Acton SP2150 spectrograph/monochromator and a tungsten lamp used for illumination.

(Time Resolved) Photoluminescence. Steady-state PL spectra were recorded with an Acton SP2150 spectrograph/monochromator with an InGaAs femtowatt photoreceiver 2153 (Newport). For time-resolved measurements covering time scales up to the μs range we used a μ-PL setup with a microscope objective which is focusing the laser beam as well as collecting the PL signal emitted by the sample. The sample was excited by a pulsed laser with a wavelength of 657 nm, a pulse width <200 ps and an average optical power of 150 μW. The time delayed PL signal was detected by a superconducting single photon detector (SSPD) from Scontel, operated at 1.8 K, which allows single photon detection with a quantum efficiency of

approximately 12% (at $\lambda = 1.31\ \mu$m) and a counting rate larger than 70 MHz. For acquisition of the decay curves the time-correlated single photon counting (TCSPC) system PicoHarp 300 by PicoQuant was used which records the arrival times of single photons detected by the SSPD relative to the excitation laser pulse times (start−stop times). The time resolution of the measurements presented in this work was 64 ps at an excitation pulse rate of 1 MHz.

Pump−Probe. experiments were performed with a pump at $\lambda = 532$ nm, $\tau_p = 10$ ps, $E_p = 200\ \mu$J, $\nu = 5$ kHz, provided from a Duettino laser (Time Bandwidth), which was electronically synchronized with to the probe. The probe was provided by an IR LED, emitting at $\lambda = 1440$ nm, pulses with a duration of $\tau_p = 10\ \mu$s. The probe was recorded by a InGaAs photodiode. The probe was modulated with mechanical chopper in order to avoid drift artifacts. The signal was recovered with a SR830 (Stanford Research) lock-in amplifier. The synchronization and delay between pump and probe pulses were controlled by standard electronic pulse generator.

Photoinduced Absorption. Induced by a CW diode pumped solid state (DPSS) laser, emitting at a wavelength of 532 nm, electronically modulated by square pulses in a frequency range between 40 Hz and 20 kHz. The absorbance was measured with light from a tungsten lamp, monochromized by an Acton SP2150 monochromator. Detected was the light by a liquid nitrogen cooled InGaAs detector. The laser modulated signal of the photoinduced absorption was collected by a SR830 Stanford Research lock-in. PL spectra were recorded in the same setup in order to evaluate the range of possible artifacts to the PIA spectrum due to emission, which does not exceed noise level in all spectra taken.

Conflict of Interest: The authors declare no competing financial interest.

Acknowledgment. We thank the Austrian Science fund FWF for financial support *via* the SFB project IR_ON. M.K. and S.Y. acknowledge financial support from the European Union through the FP7 (ERC Starting Grant NANOSOLID, GA No. 306733). W.H. gratefully acknowledges use of the services and facilities of the "Energie Campus Nürnberg" and financial support through the "Aufbruch Bayern" initiative of the state of Bavaria. Authors thank Sonja Roters, Ekkehard Nusko and Wolfgang Grafeneder for technical assistance and Dr. Nicholas Stadie for reading the manuscript.

Supporting Information Available: Supporting Figures S1−S13 including HRTEM images, light intensity dependences of the photoresponsivity for short pulses, luminescence spectra, experimental setups for the PIA and pump−probe measurements, trap state distribution upon oxidation, photoconductivity phase spectra, trap state distribution and its approximation with a model function, transistor characteristics in dark and under illumination. Further, the solution of the rate equation is given in detail. This material is available free of charge *via* the Internet at http://pubs.acs.org.

REFERENCES AND NOTES

1. Lee, J. S.; Kovalenko, M. V.; Huang, J.; Chung, D. S.; Talapin, D. V. Band-like Transport, High Electron Mobility and High Photoconductivity in All-Inorganic Nanocrystal Arrays. *Nat. Nanotechnol.* **2011**, *6*, 348–352.
2. Konstantatos, G.; Clifford, J.; Levina, L.; Sargent, E. H. Sensitive Solution-Processed Visible-Wavelength Photodetectors. *Nat. Photonics* **2007**, *1*, 531–534.
3. Lhuillier, E.; Robin, A.; Ithurria, S.; Aubin, H.; Dubertret, B. Electrolyte-Gated Colloidal Nanoplatelets-Based Phototransistor and Its Use for Bicolor Detection. *Nano Lett.* **2014**, *14*, 2715–2719.
4. Lu, M. L.; Lai, C. W.; Pan, H. J.; Chen, C. T.; Chou, P. T.; Chen, Y. F. A Facile Integration of Zero- (I-III-VI Quantum Dots) and One-(Single SnO_2 Nanowire) Dimensional Nanomaterials: Fabrication of a Nanocomposite Photodetector with Ultrahigh Gain and Wide Spectral Response. *Nano Lett.* **2013**, *13*, 1920–1927.
5. Lhuillier, E.; Keuleyan, S.; Liu, H.; Guyot-Sionnest, P. Mid-IR Colloidal Nanocrystals. *Chem. Mater.* **2013**, *25*, 1272–1282.
6. Chen, G.; Liang, B.; Liu, X.; Liu, Z.; Yu, G.; Xie, X. M.; Luo, T.; Chen, D.; Zhu, M. Q.; *et al.* High-Performance Hybrid Phenyl-C_{61}-Butyric Acid Methyl Ester/Cd_3P_2 Nanowire Ultraviolet-Visible-Near Infrared Photodetectors. *ACS Nano* **2014**, *8*, 787–796.
7. Lhuillier, E.; Keuleyan, S.; Zolotavin, P.; Guyot-Sionnest, P. Mid-Infrared HgTe/As_2S_3 Field Effect Transistors and Photodetectors. *Adv. Mater.* **2013**, *25*, 137–141.
8. Konstantatos, G.; Howard, I.; Fischer, A.; Hoogland, S.; Clifford, J.; Klem, E.; Levina, L.; Sargent, E. H. Ultrasensitive Solution-Cast Quantum Dot Photodetectors. *Nature* **2006**, *442*, 180–183.
9. Rauch, T.; Boberl, M.; Tedde, S. F.; Furst, J.; Kovalenko, M. V.; Hesser, G.; Lemmer, U.; Heiss, W.; Hayden, O. Near-Infrared Imaging with Quantum-Dot-Sensitized Organic Photodiodes. *Nat. Photonics* **2009**, *3*, 332–336.
10. Keuleyan, S.; Lhuillier, E.; Brajuskovic, V.; Guyot-Sionnest, P. Mid-Infrared HgTe Colloidal Quantum Dot Photodetectors. *Nat. Photonics* **2011**, *5*, 489–493.
11. Konstantatos, G.; Levina, L.; Tang, J.; Sargent, E. H. Sensitive Solution-Processed Bi_2S_3 Nanocrystalline Photodetectors. *Nano Lett.* **2008**, *8*, 4002–4006.
12. Lhuillier, E.; Keuleyan, S.; Liu, H.; Guyot-Sionnest, P. Colloidal HgTe Material for Low-Cost Detection into the MWIR. *J. Electron. Mater.* **2012**, *41*, 2725–2729.
13. Yarema, M.; Pichler, S.; Sytnyk, M.; Seyrkammer, R.; Lechner, R. T.; Fritz-Popovski, G.; Jarzab, D.; Szendrei, K.; Resel, R.; Korovyanko, O.; *et al.* Infrared Emitting and Photoconducting Colloidal Silver Chalcogenide Nanocrystal Quantum Dots from a Silylamide-Promoted Synthesis. *ACS Nano* **2011**, *5*, 3758–3765.
14. Chen, M. Y.; Yu, H.; Kershaw, S. V.; Xu, H. H.; Gupta, S.; Hetsch, F.; Rogach, A. L.; Zhao, N. Fast, Air-Stable Infrared Photodetectors based on Spray-Deposited Aqueous HgTe Quantum Dots. *Adv. Funct. Mater.* **2014**, *24*, 53–59.
15. Clifford, J. P.; Konstantatos, G.; Johnston, K. W.; Hoogland, S.; Levina, L.; Sargent, E. H. Fast, Sensitive and Spectrally Tuneable Colloidal Quantum-Dot Photodetectors. *Nat. Nanotechnol.* **2009**, *4*, 40–44.
16. Liu, Y. W.; Ko, D. K.; Oh, S. J.; Gordon, T. R.; Vicky, D. N.; Paik, T.; Kang, Y. J.; Ye, X. C.; Jin, L. H.; Kagan; *et al.* Near-Infrared Absorption of Monodisperse Silver Telluride (Ag_2Te) Nanocrystals and Photoconductive Response of Their Self-Assembled Superlattices. *Chem. Mater.* **2011**, *23*, 4657–4659.
17. Rogach, A. L.; Eychmuller, A.; Hickey, S. G.; Kershaw, S. V. Infrared-Emitting Colloidal Nanocrystals: Synthesis, Assembly, Spectroscopy, and Applications. *Small* **2007**, *3*, 536–557.
18. Kovalenko, M. V.; Kaufmann, E.; Pachinger, D.; Roither, J.; Huber, M.; Stangl, J.; Hesser, G.; Schaffler, F.; Heiss, W. Colloidal HgTe Nanocrystals with Widely Tunable Narrow Band Gap Energies: From Telecommunications to Molecular Vibrations. *J. Am. Chem. Soc.* **2006**, *128*, 3516–3517.
19. Keuleyan, S.; Lhuillier, E.; Guyot-Sionnest, P. Synthesis of Colloidal HgTe Quantum Dots for Narrow Mid-IR Emission and Detection. *J. Am. Chem. Soc.* **2011**, *133*, 16422–16424.
20. Kershaw, S. V.; Susha, A. S.; Rogach, A. L. Narrow Bandgap Colloidal Metal Chalcogenide Quantum Dots: Synthetic Methods, Heterostructures, Assemblies, Electronic and Infrared Optical Properties. *Chem. Soc. Rev.* **2013**, *42*, 3033–3087.
21. Hinds, S.; Levina, L.; Klem, E. J. D.; Konstantatos, G.; Sukhovatkin, V.; Sargent, E. H. Smooth-Morphology Ultrasensitive Solution-Processed Photodetectors. *Adv. Mater.* **2008**, *20*, 4398–4402.
22. Pattantyus-Abraham, A. G.; Kramer, I. J.; Barkhouse, A. R.; Wang, X.; Konstantatos, G.; Debnath, R.; Levina, L.; Raabe, I.; Nazeeruddin, M. K.; Grätzel, M.; *et al.* Depleted-Heterojunction Colloidal Quantum Dot Solar Cells. *ACS Nano* **2010**, *4*, 3374–3380.
23. Klem, E. J. D.; Shukla, H.; Hinds, S.; MacNeil, D. D.; Levina, L.; Sargent, E. H. Impact of Dithiol Treatment and Air

Annealing on the Conductivity, Mobility, and Hole Density in PbS Colloidal Quantum Dot Solids. *Appl. Phys. Lett.* **2008**, *92*, 212105.
24. Barkhouse, D. A. R.; Pattantyus-Abraham, A. G.; Levina, L.; Sargent, E. H. Thiols Passivate Recombination Centers in Colloidal Quantum Dots Leading to Enhanced Photovoltaic Device Efficiency. *ACS Nano* **2008**, *2*, 2356–2362.
25. Liu, Y.; Gibbs, M.; Puthussery, J.; Gaik, S.; Ihly, R.; Hillhouse, H. W.; Law, M. Dependence of Carrier Mobility on Nanocrystal Size and Ligand Length in PbSe Nanocrystal Solids. *Nano Lett.* **2010**, *10*, 1960–1969.
26. Yu, D.; Wang, C. J.; Guyot-Sionnest, P. n-Type Conducting CdSe Nanocrystal Solids. *Science* **2003**, *300*, 1277–1280.
27. Gao, Y. N.; Aerts, M.; Sandeep, C. S. S.; Talgorn, E.; Savenije, T. J.; Kinge, S.; Siebbeles, L. D. A.; Houtepen, A. J. Photoconductivity of PbSe Quantum-Dot Solids: Dependence on Ligand Anchor Group and Length. *ACS Nano* **2012**, *6*, 9606–9614.
28. Law, M.; Luther, J. M.; Song, O.; Hughes, B. K.; Perkins, C. L.; Nozik, A. J. Structural, Optical, and Electrical Properties of PbSe Nanocrystal Solids Treated Thermally or with Simple Amines. *J. Am. Chem. Soc.* **2008**, *130*, 5974–5985.
29. Sarasqueta, G.; Choudhury, K. R.; So, F. Effect of Solvent Treatment on Solution-Processed Colloidal PbSe Nanocrystal Infrared Photodetectors. *Chem. Mater.* **2010**, *22*, 3496–3501.
30. Talapin, D. V.; Murray, C. B. PbSe Nanocrystal Solids for n- and p-Channel Thin Film Field-Effect Transistors. *Science* **2005**, *310*, 86–89.
31. Williams, K. J.; Tisdale, W. A.; Leschkies, K. S.; Haugstad, G.; Norris, D. J.; Aydil, E. S.; Zhu, X. Y. Strong Electronic Coupling in Two-Dimensional Assemblies of Colloidal PbSe Quantum Dots. *ACS Nano* **2009**, *3*, 1532–1538.
32. Boberl, M.; Kovalenko, M. V.; Gamerith, S.; List, E. J. W.; Heiss, W. Inkjet-Printed Nanocrystal Photodetectors Operating up to 3um Wavelengths. *Adv. Mater.* **2007**, *19*, 3574–3578.
33. Liu, Y.; Tolentino, J.; Gibbs, M.; Ihly, R.; Perkins, C. L.; Liu, Y.; Crawford, N.; Hemminger, J. C.; Law, M. PbSe Quantum Dot Field-Effect Transistors with Air-Stable Electron Mobilities above 7 $cm^2 V^{-1} s^{-1}$. *Nano Lett.* **2013**, *13*, 1578–1587.
34. Chuang, C.-H. M.; Brown, P. R.; Bulović, V.; Bawendi, M. G. Improved Performance and Stability in Quantum Dot Solar Cells through Band Alignment Engineering. *Nat. Mater.* **2014**, *13*, 796–801.
35. Zhitomirsky, D.; Voznyy, O.; Levina, L.; Hoogland, S.; Kemp, K. W.; Ip, A. H.; Thon, S. M.; Sargent, E. H. Engineering Colloidal Quantum Dot Solids within and beyond the Mobility-Invariant Regime. *Nat. Commun.* **2014**, *5*, 3803.
36. Dirin, D. N.; Dreyfuss, S.; Bodnarchuk, M. I.; Nedelcu, G.; Papagiorgis, P.; Itskos, G.; Kovalenko, M. V. Lead Halide Perovskites and Other Metal Halide Complexes As Inorganic Capping Ligands for Colloidal Nanocrystals. *J. Am. Chem. Soc.* **2014**, *136*, 6550–6553.
37. Kovalenko, M. V.; Bodnarchuk, M. I.; Talapin, D. V. Nanocrystal Superlattices with Thermally Degradable Hybrid Inorganic–Organic Capping Ligands. *J. Am. Chem. Soc.* **2010**, *132*, 15124–15126.
38. Kovalenko, M. V.; Scheele, M.; Talapin, D. V. Colloidal Nanocrystals with Molecular Metal Chalcogenide Surface Ligands. *Science* **2009**, *324*, 1417–1420.
39. Nag, A.; Kovalenko, M. V.; Lee, J.-S.; Liu, W.; Spokoyny, B.; Talapin, D. V. Metal-free Inorganic Ligands for Colloidal Nanocrystals: S^{2-}, HS^-, Se^{2-}, HSe^-, Te^{2-}, HTe^-, TeS_3^{2-}, OH^-, and NH^{2-} as Surface Ligands. *J. Am. Chem. Soc.* **2011**, *133*, 10612–10620.
40. Tang, J.; Kemp, K. W.; Hoogland, S.; Jeong, K. S.; Liu, H.; Levina, L.; Furukawa, M.; Wang, X.; Debnath, R.; Cha, D.; *et al.* Colloidal-Quantum-Dot Photovoltaics Using Atomic-Ligand Passivation. *Nat. Mater.* **2011**, *10*, 765–771.
41. Niu, G.; Wang, L.; Gao, R.; Ma, B.; Dong, H.; Qiu, Y. Inorganic Iodide Ligands in Ex Situ PbS Quantum Dot Sensitized Solar Cells with I^-/I_3^- Electrolytes. *J. Mater. Chem.* **2012**, *22*, 16914–16919.
42. Ning, Z.; Ren, Y.; Hoogland, S.; Voznyy, O.; Levina, L.; Stadler, P.; Lan, X.; Zhitomirsky, D.; Sargent, E. H. All-Inorganic Colloidal Quantum Dot Photovoltaics Employing Solution-Phase Halide Passivation. *Adv. Mater.* **2012**, *24*, 6295–6299.
43. Jiang, C.; Lee, J.-S.; Talapin, D. V. Soluble Precursors for $CuInSe_2$, $CuIn_{1-x}GaxSe_2$, and $Cu_2ZnSn(S,Se)_4$ Based on Colloidal Nanocrystals and Molecular Metal Chalcogenide Surface Ligands. *J. Am. Chem. Soc.* **2012**, *134*, 5010–5013.
44. Liu, W.; Lee, J. S.; Talapin, D. V. III-V Nanocrystals Capped with Molecular Metal Chalcogenide Ligands: High Electron Mobility and Ambipolar Photoresponse. *J. Am. Chem. Soc.* **2013**, *135*, 1349–1357.
45. Kovalenko, M. V.; Schaller, R. D.; Jarzab, D.; Loi, M. A.; Talapin, D. V. Inorganically Functionalized PbS–CdS Colloidal Nanocrystals: Integration into Amorphous Chalcogenide Glass and Luminescent Properties. *J. Am. Chem. Soc.* **2012**, *134*, 2457–2460.
46. Tsokkou, D.; Papagiorgis, P.; Protesescu, L.; Kovalenko, M. V.; Choulis, S. A.; Christofides, C.; Itskos, G.; Othonos, A. Photophysics of PbS Quantum Dot Films Capped with Arsenic Sulfide Ligands. *Adv. Energy Mater.* **2014**, *4*, 1301547.
47. Fafarman, A. T.; Koh, W.-K.; Diroll, B. T.; Kim, D. K.; Ko, D.-K.; Oh, S. J.; Ye, X.; Doan-Nguyen, V.; Crump, M. R.; Reifsnyder, D. C.; *et al.* Thiocyanate-Capped Nanocrystal Colloids: Vibrational Reporter of Surface Chemistry and Solution-Based Route to Enhanced Coupling in Nanocrystal Solids. *J. Am. Chem. Soc.* **2012**, *133*, 15753–15761.
48. Carrete, A.; Shavel, A.; Fontane, X.; Montserrat, J.; Fan, J. D.; Ibanez, M.; Saucedo, E.; Perez-Rodriguez, A.; Cabot, A. Antimony-Based Ligand Exchange To Promote Crystallization in Spray-Deposited $Cu_2ZnSnSe_4$ Solar Cells. *J. Am. Chem. Soc.* **2013**, *135*, 15982–15985.
49. Zhang, H.; Jang, J.; Liu, W.; Talapin, D. V. Colloidal Nanocrystals with Inorganic Halide, Pseudohalide, and Halometallate Ligands. *ACS Nano* **2014**, *8*, 7359–7369.
50. Choi, J.-H.; Fafarman, A. T.; Oh, S. J.; Ko, D.-K.; Kim, D. K.; Diroll, B. T.; Muramoto, S.; Gillen, J. G.; Murray, C. B.; Kagan, C. R. Bandlike Transport in Strongly Coupled and Doped Quantum Dot Solids: A Route to High-Performance Thin-Film Electronics. *Nano Lett.* **2012**, *12*, 2631–2638.
51. Koh, W.-k.; Saudari, S. R.; Fafarman, A. T.; Kagan, C. R.; Murray, C. B. Thiocyanate-Capped PbS Nanocubes: Ambipolar Transport Enables Quantum Dot Based Circuits on a Flexible Substrate. *Nano Lett.* **2011**, *11*, 4764–4767.
52. Chung, D. S.; Lee, J.-S.; Huang, J.; Nag, A.; Ithurria, S.; Talapin, D. V. Low Voltage, Hysteresis Free, and High Mobility Transistors from All-Inorganic Colloidal Nanocrystals. *Nano Lett.* **2012**, *12*, 1813–1820.
53. Rowland, C. E.; Liu, W.; Hannah, D. C.; Chan, M. K. Y.; Talapin, D. V.; Schaller, R. D. Thermal Stability of Colloidal InP Nanocrystals: Small Inorganic Ligands Boost High-Temperature Photoluminescence. *ACS Nano* **2013**, *8*, 977–985.
54. Zhang, H.; Hu, B.; Sun, L.; Hovden, R.; Wise, F. W.; Muller, D. A.; Robinson, R. D. Surfactant Ligand Removal and Rational Fabrication of Inorganically Connected Quantum Dots. *Nano Lett.* **2011**, *11*, 5356–5361.
55. Nag, A.; Chung, D. S.; Dolzhnikov, D. S.; Dimitrijevic, N. M.; Chattopadhyay, S.; Shibata, T.; Talapin, D. V. Effect of Metal Ions on Photoluminescence, Charge Transport, Magnetic and Catalytic Properties of All-Inorganic Colloidal Nanocrystals and Nanocrystal Solids. *J. Am. Chem. Soc.* **2012**, *134*, 13604–13615.
56. Kravchyk, K.; Protesescu, L.; Bodnarchuk, M. I.; Krumeich, F.; Yarema, M.; Walter, M.; Guntlin, C.; Kovalenko, M. V. Monodisperse and Inorganically Capped Sn and Sn/SnO_2 Nanocrystals for High-Performance Li-Ion Battery Anodes. *J. Am. Chem. Soc.* **2013**, *135*, 4199–4202.
57. Llordes, A.; Hammack, A. T.; Buonsanti, R.; Tangirala, R.; Aloni, S.; Helms, B. A.; Milliron, D. J. Polyoxometalates and Colloidal Nanocrystals as Building Blocks for Metal Oxide Nanocomposite Films. *J. Mater. Chem.* **2011**, *21*, 11631–11638.

58. Llordes, A.; Garcia, G.; Gazquez, J.; Milliron, D. J. Tunable Near-Infrared and Visible-Light Transmittance in Nanocrystal-in-Glass Composites. *Nature* **2013**, *500*, 323–326.
59. Lee, J. E.; Yu, S.-H.; Lee, D. J.; Lee, D.-C.; Han, S. I.; Sung, Y.-E.; Hyeon, T. Facile and Economical Synthesis of Hierarchical Carbon-Coated Magnetite Nanocomposite Particles and Their Applications in Lithium Ion Battery Anodes. *Energy Environ. Sci.* **2012**, *5*, 9528–9533.
60. Ocier, C. R.; Whitham, K.; Hanrath, T.; Robinson, R. D. Chalcogenidometallate Clusters as Surface Ligands for PbSe Nanocrystal Field-Effect Transistors. *J. Phys. Chem. C* **2014**, *118*, 3377–3385.
61. Jang, J.; Liu, W.; Son, J. S.; Talapin, D. V. Temperature-Dependent Hall and Field-Effect Mobility in Strongly Coupled All-Inorganic Nanocrystal Arrays. *Nano Lett.* **2014**, *14*, 653–662.
62. Zhuang, J. Q.; Wu, H. M.; Yang, Y. A.; Cao, Y. C. Supercrystalline Colloidal Particles from Artificial Atoms. *J. Am. Chem. Soc.* **2007**, *129*, 14166–14167.
63. Jang, B.; Park, M.; Chae, O. B.; Park, S.; Kim, Y.; Oh, S. M.; Piao, Y.; Hyeon, T. Direct Synthesis of Self-Assembled Ferrite/Carbon Hybrid Nanosheets for High Performance Lithium-Ion Battery Anodes. *J. Am. Chem. Soc.* **2012**, *134*, 15010–15015.
64. Kim, D. K.; Lai, Y.; Diroll, B. T.; Murray, C. B.; Kagan, C. R. Flexible and Low-Voltage Integrated Circuits Constructed from High-Performance Nanocrysal Transistors. *Nat. Commun.* **2012**, *3*, 1216.
65. Oh, S. J.; Berry, N. E.; Choi, J.-H.; Gaulding, E. A.; Lin, H.; Paik, T.; Hong, S.-H.; Murray, C. B.; Kagan, C. R. Stoichiometric Control of Lead Chalcogenide Nanocrystal Solids to Enhance Their Electronic and Optoelectronic Device Performance. *ACS Nano* **2013**, *7*, 2413–2421.
66. Oh, S. J.; Berry, N. E.; Choi, J.-H.; Gaulding, E. A.; Lin, H.; Paik, T.; Diroll, B. T.; Muramoto, S.; Murray, C. B.; Kagan, C. R. Designing High-Performance PbS and PbSe Nanocrystal Electronic Devices through Stepwise, Post-Synthesis, Colloidal Atomic Layer Deposition. *Nano Lett.* **2014**, *14*, 1559–1566.
67. Liao, J. H.; Varotsis, C.; Kanatzidis, M. G. Syntheses, Structures, and Properties of 6 Novel Alkali-Metal Tin Sulfides—K_2Sn_2S8, Alpha-$Rb_2Sn_2S_8$, Beta-$Rb_2Sn_2S_8$, $K_2Sn_2S_5$, $Cs_2Sn_2S_6$, and Cs_2SnS_{14}. *Inorg. Chem.* **1993**, *32*, 2453–2462.
68. Wang, R. Y.; Tangirala, R.; Raoux, S.; Jordan-Sweet, J. L.; Milliron, D. J. Ionic and Electronic Transport in Ag_2S Nanocrystal−GeS_2 Matrix Composites with Size-Controlled Ag_2S Nanocrystals. *Adv. Mater.* **2012**, *24*, 99–103.
69. Ko, D.-K.; Kang, Y.; Murray, C. B. Enhanced Thermopower *via* Carrier Energy Filtering in Solution-Processable Pt−Sb_2Te_3 Nanocomposites. *Nano Lett.* **2011**, *11*, 2841–2844.
70. Kovalenko, M. V.; Spokoyny, B.; Lee, J.-S.; Scheele, M.; Weber, A.; Perera, S.; Landry, D.; Talapin, D. V. Semiconductor Nanocrystals Functionalized with Antimony Telluride Zintl Ions for Nanostructured Thermoelectrics. *J. Am. Chem. Soc.* **2010**, *132*, 6686–6695.
71. Talapin, D. V.; Lee, J.-S.; Kovalenko, M. V.; Shevchenko, E. V. Prospects of Colloidal Nanocrystals for Electronic and Optoelectronic Applications. *Chem. Rev.* **2009**, *110*, 389–458.
72. Guyot-Sionnest, P. Electrical Transport in Colloidal Quantum Dot Films. *J. Phys. Chem. Lett.* **2012**, *3*, 1169–1175.
73. Konstantatos, G.; Levina, L.; Fischer, A.; Sargent, E. H. Engineering the Temporal Response of Photoconductive Photodetectors *via* Selective Introduction of Surface Trap States. *Nano Lett.* **2008**, *8*, 1446–1450.
74. Konstantatos, G.; Sargent, E. H. PbS Colloidal Quantum Dot Photoconductive Photodetectors: Transport, Traps, and Gain. *Appl. Phys. Lett.* **2007**, *91*, 173505.
75. Kovalenko, M. V.; Bodnarchuk, M. I.; Zaumseil, J.; Lee, J.-S.; Talapin, D. V. Expanding the Chemical Versatility of Colloidal Nanocrystals Capped with Molecular Metal Chalcogenide Ligands. *J. Am. Chem. Soc.* **2010**, *132*, 10085–10092.
76. Nagpal, P.; Klimov, V. I. Role of mid-Gap States in Charge Transport and Photoconductivity in Semiconductor Nanocrystal Films. *Nat. Commun.* **2011**, *2*, 486.
77. Munro, A. M.; Jen-La Plante, I.; Ng, M. S.; Ginger, D. S. Quantitative Study of the Effects of Surface Ligand Concentration on CdSe Nanocrystal Photoluminescence. *J. Phys. Chem. C* **2007**, *111*, 6220–6227.
78. Hines, M. A.; Scholes, G. D. Colloidal PbS Nanocrystals with Size-Tunable Near-Infrared Emission: Observation of Post-Synthesis Self-Narrowing of the Particle Size Distribution. *Adv. Mater.* **2003**, *15*, 1844–1849.
79. Moreels, I.; Justo, Y.; De Geyter, B.; Haustraete, K.; Martins, J. C.; Hens, Z. Size-Tunable, Bright, and Stable PbS Quantum Dots: A Surface Chemistry Study. *ACS Nano* **2011**, *5*, 2004–2012.
80. Sukhovatkin, V.; Hinds, S.; Brzozowski, L.; Sargent, E. H. Colloidal Quantum-Dot Photodetectors Exploiting Multiexciton Generation. *Science* **2009**, *324*, 1542–1544.
81. Bube, R. H. *Photoconductivity of Solids*; John Wiley & Sons: New York, 1978; p 461.
82. Garside, B. K.; Lim, T. K. Laser Mode Locking Using Saturable Absorbers. *J. Appl. Phys.* **1973**, *44*, 2335–2342.
83. Stassen, A. F.; de Boer, R. W. I.; Iosad, N. N.; Morpurgo, A. F. Influence of the Gate Dielectric on the Mobility of Rubrene Single-Crystal Field-Effect Transistors. *Appl. Phys. Lett.* **2004**, *85*, 3899–3901.
84. Behrens, H.; Glasser, L. Uber das Verhalten von Arsen(III)-Sulfid Gegenüber Flüssigem Ammoniak. *Z. Anorg. Allg. Chem.* **1955**, *278*, 174–183.